scientific reports

Check for updates

OPEN

Quantum neural network-based compensation of distorted orbital angular momentum beams in complex media

Gokul Manavalan✉ & Shlomi Arnon

Quantum computing is emerging as a transformative tool for communication systems, offering the potential to overcome long-standing physical limitations. In free-space optical networks, orbital angular momentum (OAM) multiplexing promises massive capacity gains, but its practical use is fundamentally constrained by multiphysics degradations such as atmospheric turbulence, volumetric Mie scattering, and stochastic quantum noise. These effects induce nonlinear modal crosstalk and severe beam distortions, against which classical approaches—most notably convolutional neural networks (CNNs)—provide only partial and non-scalable compensation. To address this gap, we report the first use of variational quantum neural networks (QNNs) for adaptive OAM beam compensation in realistic channels. By embedding parameterized entangling layers into a supervised regression pipeline, our QNN achieves end-to-end reconstruction of distorted Laguerre–Gaussian beams with topological charges $l \in \{1,4,8,12\}$. Using experimentally validated channel parameters, QNNs achieve mean squared error as low as 4.0×10^{-6}, SSIM above 0.99, and bit-error rates suppressed by >99.9% (0.0125% BER). To ensure scalability, we introduce the quasi-quantum neural network (QqNN), a classical surrogate that emulates quantum dynamics via tensorial projections, achieving near-optimal performance (0.0375% BER) at reduced complexity. This hybrid framework positions QNNs as a quantum-resilient paradigm for OAM decoding and establishes QqNNs as the first scalable surrogate for near-term deployment.

Quantum algorithms and quantum computing are rapidly emerging as transformative paradigms in information processing, with particular promise for communication systems where classical methods struggle to address complex optimization and signal restoration tasks[1–4]. Among the most compelling frontiers is the mitigation of channel impairments in high-dimensional photonic communication schemes. Within this context, orbital angular momentum (OAM) of light has attracted significant attention as a carrier of information due to its theoretically unbounded Hilbert space and compatibility with both free-space and guided-wave architectures[5–8]. However, the practical viability of OAM-based systems critically depends on developing robust methods to counteract multiphysics degradations—including atmospheric turbulence, volumetric scattering, and stochastic quantum decoherence—that induce modal crosstalk, phase scrambling, and intensity distortions[7–10].

OAM beams, characterized by the azimuthal phase factor $\exp(il\varphi)$ with topological charge l, form the basis of Laguerre–Gaussian (LG) modes that enable multiplexing across independent spatial channels[5–8]. This unique spatial structure underpins ultrahigh-capacity free-space optical (FSO) links, mode-division multiplexing in fibers, and quantum key distribution in integrated photonics[11,12]. Yet, their performance remains acutely sensitive to environmental perturbations: even moderate levels of turbulence, scattering, or decoherence can collapse modal orthogonality, leading to catastrophic fidelity loss in both free-space and guided-wave platforms[7–10]. Overcoming these impairments requires compensation strategies capable of addressing the inherently nonlocal and multiphysics nature of OAM distortions.

Recent advances have explored classical and physics-informed neural network architectures for OAM beam compensation[13–17]. Guo et al.[16] proposed a hybrid forecasting mechanism based on two-stage variational mode decomposition and autoregressive modeling (TsVMD-AR), targeting turbulence prediction via temporal modeling of Fried parameter fluctuations[16]. Jia et al.[13] extended the paradigm to spatial domain restoration, employing a dissipative diffractive deep neural network (D2NN) architecture, where the compensation process exploits spatial mode filtering via learnable optical transfer functions[13]. Zhang et al.[18] introduced a sensorless

Electrical and Computer Engineering department of Ben-Gurion University of the Negev, 8441405 Be'er Sheva, Israel. ✉email: gokulm@post.bgu.ac.il

adaptive optics (AO) framework utilizing Pix2PixGANs to perform image-to-image translation from distorted to corrected vortex modes, demonstrating efficacy across high-data-rate OAM-FSO links under strong turbulence, with potential extensions to mode-division multiplexed fibers where intermodal crosstalk similarly limits capacity[18]. While impactful, these methods fundamentally rely on local correlations in distorted intensity space, limiting their ability to capture the nonlocal, multiphysics couplings underlying OAM degradation.

Concurrently, quantum machine learning (QML) has emerged as a compelling approach for extracting globally entangled representations in high-dimensional signal spaces[2–4]. Parametric quantum neural networks (QNNs), in particular, offer exponentially rich hypothesis classes via variational circuit learning, enabling global feature extraction through entanglement and non-classical kernel embeddings[19,20]. Larocca et al. rigorously characterized the overparameterization phase transition in QNNs, showing that expressivity sharply increases once a critical operator rank is achieved[20]. This provides a theoretical basis for the use of deep variational circuits in structured signal regression. Applications of QNNs have since permeated biomedical diagnostics (Qu et al.)[21], financial time-series modeling (Paquet et al.)[22], and quantum-enhanced classification (Zhou et al.)[1], demonstrating superior generalization in noise-prone regimes. Badreddine et al.[23] pioneered the use of hybrid ConvQuantum networks for OAM mode classification under turbulence[23]. However, their work remains restricted to discrete classification tasks under single-physics turbulence. To date, no study has addressed the continuous-valued regression and compensation of intensity-deformed OAM beams under composite turbulence–scattering–decoherence channels. Moreover, the computational cost of full quantum pipelines under idealized, noise-free simulations poses a scalability bottleneck, motivating development of tractable, quantum-inspired surrogates.

In this work, we introduce a variational quantum neural network (QNN) regression framework for end-to-end restoration of distorted LG beams with topological charges $l \in \{1,4,8,12\}$. While demonstrated here for free-space channels, the approach is inherently extensible to guided-wave platforms such as few-mode fibers and integrated waveguides. The QNN leverages parameterized entangling layers within a supervised learning pipeline, enabling sub-wavelength reconstruction of amplitude distributions. To address scalability challenges, we further propose a quasi-quantum neural network (QqNN)—a classical surrogate that emulates entangling dynamics through nonlinear tensor projections, achieving near-quantum performance with markedly lower computational cost. The overall workflow of beam generation, channel distortion, and QqNN-based compensation is illustrated in Fig. 1. In both simulation and experiment, the proposed QNN achieves over 99% reductions in MSE and BER with SSIM exceeding 0.99, while the QqNN delivers comparable performance with substantially reduced computational overhead. To the best of our knowledge, this constitutes the first demonstration of QNN-enabled regression and compensation of OAM beams degraded by composite turbulence, scattering, and decoherence. Beyond establishing QNNs as a quantum-resilient paradigm and QqNNs as efficient surrogates for noise-prone OAM links, this hybrid framework lays a forward-compatible foundation for quantum–classical transceiver

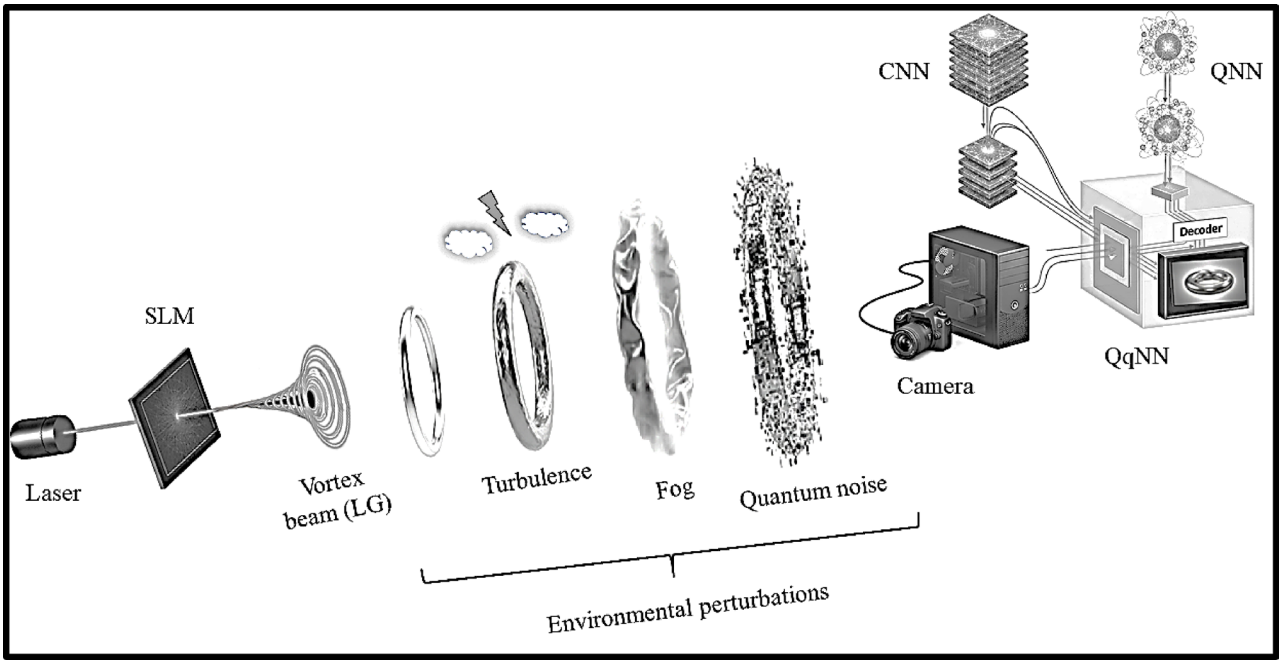

Fig. 1. Graphical abstract: A schematic representation of the proposed experimental and computational framework. A collimated laser beam is phase-modulated via a spatial light modulator (SLM) to generate a vortex (LG) mode of prescribed topological charge. The structured beam subsequently propagates through a multiphysics perturbative channel comprising atmospheric turbulence, fog-induced Mie scattering, and quantum decoherence processes. The distorted optical field is collected by a camera and digitally processed by the proposed QqNN for compensation and reconstruction.

architectures. As quantum hardware matures, such models can be natively executed on quantum processors, enabling orders-of-magnitude acceleration in training and inference for high-dimensional optical channels.

Structured light propagation through multiple physical perturbative channels

Structured light beams carrying OAM span a high-dimensional Hilbert space, offering unbounded degrees of freedom for photonic encoding[9,24,25]. In the paraxial regime, OAM-carrying beams are typically represented in the LG basis, $LG_{(p,l)}(r,\varphi,z)$, which constitutes an orthonormal set of solutions to the scalar paraxial Helmholtz equation in cylindrical coordinates[26–28]. The complex field distribution of a Laguerre–Gaussian beam is given by[9,29]:

$$\mathrm{LG}_{p,l}(r,\varphi,z) = \frac{1}{w(z)}\sqrt{\frac{2p!}{\pi\,(|l|+p)!}} * exp\left[i\,(2p+|l|+1)\,\varphi\,(z)\right] * \left(\frac{\sqrt{2}r}{w(z)}\right)^{|l|} L_p^{|l|}\left(\frac{2r^2}{w(z)^2}\right) * \exp\left(-\frac{ikr^2}{2R(z)}\right)\exp\left(-\frac{r^2}{w(z)^2}\right)\exp(il\varphi) \quad (1)$$

Here, $w(z) = w_0\sqrt{1+{z^2}/{z_R^2}}$ represents the beam waist at axial distance z, where w_0 is the waist radius at the beam focus and $z_R = \frac{\pi\, w_0^2}{\lambda}$ is the Rayleigh range. The radius of curvature of the beam's wavefront is given by $R(z) = z\left[1+\left(\frac{z_R}{z}\right)^2\right]$, and $\varphi(z) = \arctan\left(\frac{z}{z_R}\right)$ denotes the Gouy phase shift. The radial mode index p and azimuthal index l characterize the spatial distribution, with $L_p^{|l|}(\cdot)$ being the generalized Laguerre polynomial. The wave number is $k = \frac{2\pi}{\lambda}$. This expression captures both the helical phase and radial intensity distribution of an ideal OAM mode in free-space[9,24,25]. To rigorously emulate real-world propagation environments, the structured LG modes were modeled under three independent yet cumulative perturbations: atmospheric turbulence, fog-induced multiple scattering, and quantum decoherence. Each distortion source was treated analytically and numerically to preserve physical fidelity, thereby ensuring that the subsequent machine-learning evaluation operates on data consistent with optical physics.

Atmospheric turbulence modeling

Propagation through the turbulent atmosphere introduces stochastic refractive-index fluctuations, leading to phase-front corrugation, intensity scintillation, and modal crosstalk[12,30–33]. We model turbulence via a Monte Carlo phase-screen approach, employing the modified Kolmogorov power spectral density with von Kármán inner and outer scale corrections[9,34]. A distorted LG field is given as

$$U_{turb}(x,y) = U_{in}(x,y)\,exp[j\phi_{turb}(x,y)] \quad (2)$$

Where $U_{in}(x,y)$ is the input LG beam and $\phi_{turb}(x,y)$ is a zero-mean Gaussian random phase function, whose statistics are dictated by the power spectral density (PSD)[9,34]:

$$\varphi_{\phi}(q_x,q_y) = 0.023 r_0^{-5/3}(|q|^2+\frac{1}{L_0^2})^{-11/6} exp\left(-|q|^2 l_0^2\right) \quad (3)$$

Here, r_0 is the Fried coherence diameter that quantifies the spatial correlation of phase distortions, while L_0 and l_0 are the outer and inner scales of turbulence; $q = (q_x, q_y)$ are spatial frequencies. Equation (3) defines the Fourier-domain statistics from which the random phase screen $\phi_{turb}(x,y)$ is synthesized[34,35]. Applying this phase screen to the LG field yields the turbulence-distorted field and this operation captures multi-scale phase perturbations, which induce both randomized wavefront tilts and intensity speckling, especially detrimental to higher-order OAM modes due to their extended phase gradients.

Fog induced multiple scattering

Volumetric Mie scattering in fog introduces spatial amplitude blurring and additional attenuation, which can fundamentally distort the spatial fidelity of OAM beams[10,36,37]. Fog is modeled as a diffusive, multiple-scattering channel that imposes both attenuation and spatial blurring[37,38]. Since the convolution is performed in the spatial-frequency domain, we express both the turbulence-perturbed field $U_{\mathrm{turb}}(f_x,f_y)$ and the fog transfer function $H(f_x,f_y)$ in Fourier space, such that the fog-attenuated field is given by,

$$U_{fog}(f_x,f_y) = U_{\mathrm{turb}}(f_x,f_y)\,H(f_x,f_y) \quad (4)$$

Where f_x and f_y denote the spatial frequencies, and $H(f_x,f_y)$ is a Gaussian point-spread function (PSF) inspired by the Henyey–Greenstein (HG) scattering law[38,39]. Explicitly,

$$H(f_x,f_y) = exp\left[-\frac{f_x^2+f_y^2}{2\sigma^2}\right]\cdot T \quad (5)$$

With scattering width $\sigma = \frac{1}{\lambda\, z_{fog}}\sqrt{\frac{1-g}{2}}$. Here, $g \in [0,1]$ is the HG anisotropy parameter, λ is the optical wavelength, and z_{fog} is the effective propagation distance through fog[38]. The scalar transmittance factor T accounts for exponential intensity decay,

$$T = exp(-\beta\, z_{fog}) \quad (6)$$

Where $\beta\ \left(m^{-1}\right)$ is the medium's attenuation coefficient, determined by Mie scattering cross-section and particle concentration[37,38]. Equations (4)–(6) together approximate the angular scattering statistics of the HG distribution while retaining computational tractability via a Gaussian kernel. The model captures both spatial-frequency filtering and overall transmission loss due to fog.

Quantum noise channels

Beyond classical distortions, optical beams experience quantum decoherence arising from photon loss, dephasing, and environmental coupling[40–42]. In our simulations, this is represented via stochastic Kraus-equivalent maps applied to the intensity distribution[40]. The degraded field is

$$U_{\text{final}}(x,y) = M_{\text{deph}}(x,y)\ M_{\text{loss}}(x,y)\ U_{\text{fog}}(x,y) \tag{7}$$

where $M_{\text{deph}}(x,y)$ is a multiplicative random phase mask drawn from a Bernoulli distribution with probability γ_d of phase flip (mimicking a dephasing channel)[43–45], and $M_{\text{loss}}(x,y)$ is a binary mask with transmission probability γ_l, modeling amplitude damping or photon loss[43]. This procedure effectively implements classical-field surrogates of Kraus operators[44,45]:

- $M_{\text{deph}}(x,y)$: Dephasing: $\rho \mapsto (1-\gamma_d)\rho + \gamma_d Z\rho Z$
- $M_{\text{loss}}(x,y)$: Amplitude damping: $\rho \mapsto E_0\rho E_0^\dagger + E_1\rho E_1^\dagger$

Where ρ: input quantum state density operator; Z: Pauli-Z operator; E_0, E_1: Kraus operators, $E_0 = \begin{bmatrix} 1 & 0 \\ 0 & \sqrt{\gamma_l} \end{bmatrix}$, $E_1 = \begin{bmatrix} 0 & \sqrt{1-\gamma_l} \\ 0 & 0 \end{bmatrix}$; and † indicate Hermitian conjugate[44,45]. While the Bernoulli-mask approach does not simulate multi-photon entanglement explicitly, it statistically reproduces the ensemble-averaged behavior of single-beam quantum channels (dephasing and amplitude damping). For intensity-based observables, this surrogate is equivalent to applying the corresponding Kraus maps, as shown in prior work[43–45], ensuring that simulated decoherence and photon-loss effects faithfully reflect real quantum channel statistics.

Equations (2)–(7) sequentially define the cumulative impact of turbulence, fog, and quantum noise, respectively. Together they yield the fully degraded LG beam field $U_{\text{final}}(x,y)$, which exhibits random phase corrugations, diffusive blurring, photon loss, and coherence decay. This composite model captures the salient physics of long-distance free-space optical communication channels under real-world environmental perturbations. Representative examples of distorted LG beams across different topological charges are provided in Supplementary Fig. 1. To reconstruct the fidelity of the fully perturbed field $U_{\text{final}}(x,y)$, we developed deep-learning architectures spanning both classical and quantum paradigms. Specifically, we employed CNNs, inspired by autoencoder-style encoder–decoder topologies, variational QNNs based on parametrized quantum circuits, and a hybrid QqNN that fuses classical convolutional layers with variational quantum layers.

Proposed methodology

This section delineates the comprehensive algorithmic framework, dataset curation strategy, and training protocol employed for three neural paradigms, QNN, QqNN, and CNN—designed for high-fidelity reconstruction and compensation of OAM beam profiles subjected to cumulative degradation from atmospheric turbulence, volumetric fog, and quantum noise channels. All networks are trained and validated on synthetically generated datasets with topological charges $l \in \{1,4,8,12\}$, spatial resolution of 64×64 pixels, and sufficient sample diversity to span the stochastic variability of the perturbative channels. The implementation leverages PyTorch 2.1 for classical deep learning operations, PennyLane 0.33 for variational quantum circuit simulation with automatic differentiation, and NumPy 1.26 for high-performance linear algebra[46,47]. All computations are executed on Google Colab GPU instances (NVIDIA Tesla T4/A100), ensuring rapid prototyping and end-to-end training.

Quantum neural network (QNN)

The QNN leverages a fully quantum latent embedding via a parameterized quantum circuit (PQC), enabling the extraction of globally entangled features that classical networks cannot capture efficiently (Fig. 2)[19,20]. The input image $I_{in} \in R^{1\times 64\times 64}$ is reshaped into a vector $x \in R^{4096}$ and projected into a quantum-compatible latent representation via a nonlinear transformation followed by a learnable affine mapping[48]:

$$x_q = \pi \cdot tanh(W_1 x + b_1),\ x_q \in R^{16} \tag{8}$$

where $W_1 \in R^{16\times 4096}$ and $b_1 \in R^{16}$ are trainable parameters. The use of $tanh(x)$ ensures bounded rotation angles $[-\pi, \pi]$, mitigating over-rotation in the quantum circuit[48]. The latent vector x_q is encoded into a 16-qubit quantum state using PennyLane's default.qubit simulator[49,50]. The selection of 16 qubits was determined empirically to provide an optimal balance between circuit expressivity and a tractable simulation cost.

1. *Angle Embedding*[51]: Classical features are mapped into the Hilbert space via single-qubit rotations about the Y-axis. This process ensures a unitary and reversible embedding of classical amplitudes into quantum states.

$$U_{emb}(x_q) = \otimes_{i=0}^{15} R_y\left(x_q^{(i)}\right) = \otimes_{i=0}^{15} exp(-ix_q^{(i)}Y/2) \tag{9}$$

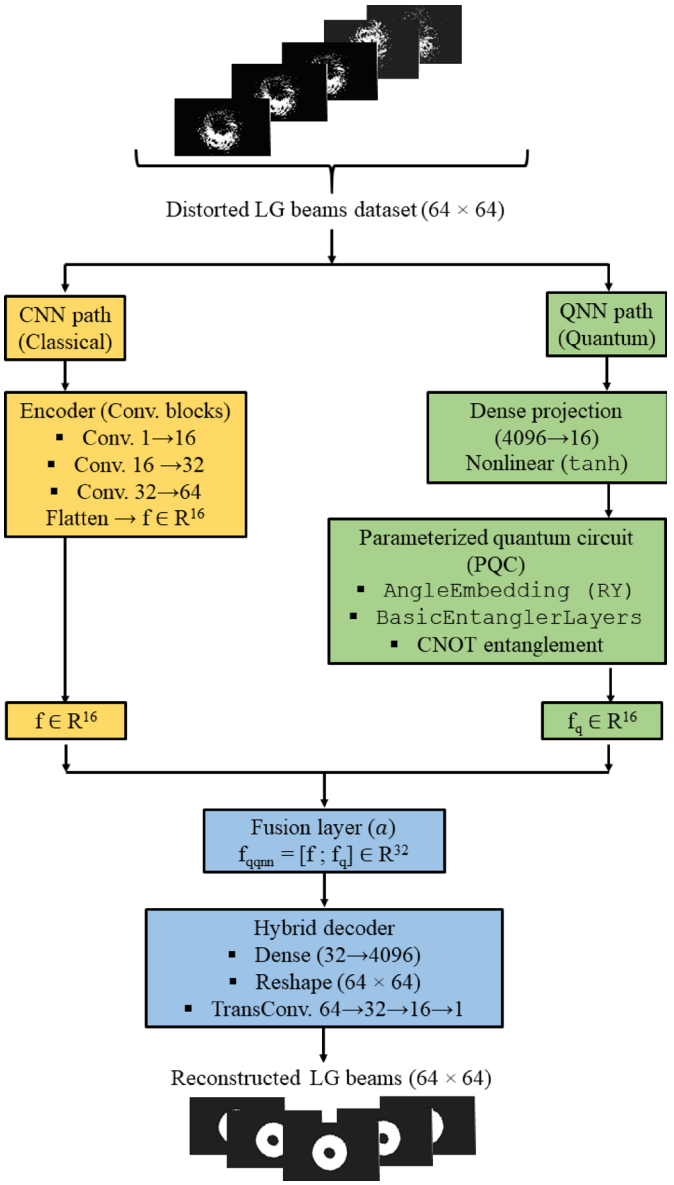

Fig. 2. Hybrid quantum–classical network architecture: Schematic of the proposed QqNN model, which integrates a classical convolutional autoencoder for feature extraction with an embedded variational quantum circuit for non-classical representation learning. The quantum block is parameterized by trainable rotation gates and entangling layers, enabling nonlinear feature fusion that enhances robustness against channel-induced distortions.

This operation ($\otimes$) signifies a tensor product, which represents the independent application of the single-qubit rotations to each of the 16 qubits, thereby encoding the classical features into the combined quantum state.

2. *Variational Ansatz (BasicEntanglerLayers)*[52]: To generate entanglement and capture nonlocal correlations across qubits, a hardware-efficient ansatz is employed:

$$U_{var}(\Theta) = \prod_{d=1}^{2} \left(\otimes_{i=0}^{15} R_y\left(\theta_{d,i}\right) \cdot \epsilon_{nn} \right) \tag{10}$$

Where $\Theta \in R^{2\times 16}$ are learnable variational parameters and ϵ_{nn} denotes a nearest-neighbor entanglement pattern, ensuring scalable qubit connectivity while avoiding barren plateaus in training. The composite quantum operation applied to the embedded latent vector is therefore:

$$U(x_q, \Theta) = U_{var}(\Theta) \cdot U_{emb}(x_q) \tag{11}$$

3. *Measurement and reconstruction Layer*: Following evolution through the variational circuit, Pauli-Z expectation values are measured on all qubits to collapse the quantum state into a classical latent representation[53]:

$$z = [\langle z_0 \rangle, \langle z_1 \rangle, ..., \langle z_{15} \rangle]^T \in R^{16} \tag{12}$$

These observables encode global, entangled correlations in the input beam, which are subsequently decoded into an image via a fully connected linear transformation:

$$\widehat{I} = Reshape(W_2 z + b_2), W_2 \in R^{4096 \times 16}, b_2 \in R^{4096} \tag{13}$$

All parameters $\{W_1, b_1, W_2, b_2, \Theta\}$ are optimized end-to-end via gradient descent, with quantum gradients computed using PennyLane's parameter-shift rule and propagated through PyTorch's automatic differentiation engine[46,47].

Convolutional neural network (CNN)

As a fully classical baseline, the CNN adopts a symmetric autoencoder architecture consisting of an encoder-decoder stack of convolutional and transposed convolutional layers[54,55]. The encoder channel progression is: $\{1 \rightarrow 16 \rightarrow 32 \rightarrow 64\}$, with LeakyReLU activations after each convolutional layer (Fig. 2). The decoder mirrors the encoder with transposed convolutions, reconstructing the spatial amplitude profile of the beam. The network is trained to minimize the pixel-wise mean squared error (MSE):

$$\mathcal{L}_{MSE} = \frac{1}{N} \sum_{i=1}^{N} || F_{CNN}(I_{in}^{(i)}; \theta) - I_{GT}^{(i)} ||_2^2 \tag{14}$$

Where F_{CNN} denotes the CNN mapping function and θ its parameters. While effective at capturing local correlations, CNNs lack the ability to model nonlocal entanglement patterns, limiting compensation fidelity for higher-order OAM modes under multiphysics degradation.

Quasi-quantum neural network (QqNN)

The QqNN constitutes a hybrid quantum-classical architecture, embedding a quantum variational circuit within a classical convolutional autoencoder to leverage both local and global features. The architectural design of the proposed QqNN is detailed in Fig. 2. The encoder contains three convolutional layers (3×3 kernels) with ReLU activations, progressively increasing channels $\{1 \rightarrow 16 \rightarrow 32 \rightarrow 64\}$), followed by a flattening operation and a fully connected projection into a latent feature vector $f \in R^{16}$. This classical latent vector is mapped into a quantum state via AngleEmbedding[51], processed through the same BasicEntanglerLayers[52] ansatz as in the QNN, and measured to yield a quantum-enhanced feature vector $f_q \in R^{16}$. The hybrid latent vector is then formed by concatenation:

$$f_{hybrid} = [f; f_q] \in R^{32} \tag{15}$$

The decoder reconstructs the beam profile through three transposed convolutional layers. To balance the contributions of classical and quantum components adaptively, a fusion loss is employed:

$$\mathcal{L}_{fusion} = a \cdot \mathcal{L}_{quantum} + (1 - a) \cdot \mathcal{L}_{classical} \tag{16}$$

where $\in [0,1]$ is a learnable scalar optimized alongside network parameters. This mechanism allows the network to dynamically allocate information flow between the quantum and classical channels, enhancing reconstruction fidelity under severe turbulence, scattering, and decoherence.

System parameters and evaluation

The dataset underpinning the reconstruction task was generated through rigorous numerical simulations of LG beams subjected to realistic free-space channel degradations. While Sect. II develops the analytical and computational foundations of turbulence, fog scattering, and quantum noise, this section specifies the exact parameterization adopted for dataset construction, along with the subsequent training hyperparameters and BER evaluation pipeline.

Channel distortion modeling parameters

Simulations were carried out for LG beams of azimuthal indices $l \in \{1,4,8,12\}$, each normalized to a beam waist of w_0 = 0.05 m and wavelength $\lambda = 637$ nm. A propagation length of 500 m was assumed, within which the following distortion models were instantiated:

- *Atmospheric turbulence*: Phase perturbations were synthesized using a multi-layer split-step Fourier propagation method with random Kolmogorov phase screens. The Fried parameter was set to $r_0 = 0.017$, corresponding to a strong turbulence regime. An inner scale of $l_0 = 0.01$ m and outer scale of $L_0 = 100$ m were enforced to ensure statistical consistency with the von Kármán spectrum[9,34,35].
- *Fog scattering*: Medium-induced attenuation and angular broadening were simulated via the Henyey–Greenstein phase function with anisotropy factor = 0.8. The extinction coefficient was chosen as $\beta = 0.07824$ m^{-1}, corresponding to a visibility of 50 m as per Koschmieder's law[56]. To emulate volumetric scattering, the total propagation path of 100 m was discretized into 10 scattering planes separated by 10 m.
- *Quantum noise*: To incorporate non-classical impairments, stochastic Pauli channels were applied on the simulated field. Specifically, dephasing noise with probability $\gamma_d = 0.2$ and amplitude-damping noise with probability $\gamma_l = 0.1$ were applied on a pixel-resolved basis, thereby reproducing the statistical decoherence of field modes under realistic quantum-limited detection conditions.

This parameterization ensures that the dataset captures a non-trivial interplay of deterministic diffraction, random turbulence, mesoscale scattering, and quantum-level noise, forming a stringent benchmark for hybrid quantum–classical learning models. The employed turbulence (0 = 0.017 m) and fog scattering (= 0.07824 m − 1) correspond to high-distortion conditions. Since beam degradation scales with turbulence strength and scattering[57–59], networks trained under such severe regimes are expected to generalize effectively to weaker channels exhibiting reduced phase perturbations and attenuation. For conditions far beyond this range, retraining or fine-tuning may be required to preserve reconstruction accuracy.

Dataset and hyperparameters for training

For each topological charge class, 1000 paired images of ground-truth and distorted LG beams were generated, yielding a total of 4000 distorted inputs and 4000 ground-truth targets. All images were stored in both .png and .npy formats to support classical and quantum neural network pipelines. The dataset was organized into class-wise folders, and each image was normalized to [0,1] prior to training. Dynamic loading and augmentation (random crop and intensity jitter) were implemented using torchvision.transforms to improve generalization. For each topological charge, the dataset of 1000 paired images were randomly partitioned into 70% training, 15% validation, and 15% test sets. Training, validation, and testing were conducted independently for simulation and experimental datasets to ensure statistical separation and prevent data leakage. No cross-domain fine-tuning was applied. This separation strategy is consistent with recent best practices in simulation-to-experiment modeling[60,61]. Validation subsets were used exclusively for early stopping and hyperparameter optimization. Identical splitting and augmentation strategies were employed for CNN, QNN, and QqNN to preserve fairness of comparison. Training employed the Adam optimizer with learning rate 2×10^{-4}, momentum parameters $\beta_1 = 0.5$, $\beta_2 = 0.999$, and batch size of 4. Each network was trained for 20 epochs, with early stopping enabled via validation loss. Classical CNN layers were trained using PyTorch's automatic differentiation. Quantum layers (variational circuits with AngleEmbedding and BasicEntanglerLayers) employed PennyLane's parameter-shift rule to compute gradients. Hybrid QqNN layers leveraged joint optimization, with a weighted loss fusion ensuring numerical stability between classical and quantum parameter updates. GPU acceleration was used for classical components, while quantum layers executed on the Pennylane default.qubit simulator backend.

To rigorously assess computational complexity, we evaluated three key metrics: the number of trainable parameters, average training time per epoch, and inference latency per test batch. These results, as shown in Table 1, were recorded for all three models under identical hardware conditions (NVIDIA Tesla T4 GPU). The CNN baseline consisted of approximately 1.2×10^5 parameters, with training and inference times of 0.8 s per epoch and 0.12 s per batch, respectively. The purely quantum QNN model had $\sim 7.3 \times 10^4$ parameters but incurred higher computational cost, requiring 2.6 s per epoch and 0.38 s per batch. In contrast, the hybrid QqNN model maintained a balanced profile, with $\sim 9.1 \times 10^4$ parameters, a moderate training time of 1.7 s per epoch, and an inference latency of 0.20 s per batch. Notably, quantum simulation accounted for ~60% of the QqNN's inference time. All models were trained and evaluated under identical hardware and optimization conditions to ensure fairness in comparison. These results underscore the QqNN's advantageous trade-off, offering significantly improved reconstruction fidelity over classical and quantum baselines while maintaining computational demands within a practical and efficient range. A detailed tutorial outlining the full implementation pipeline, including dataset handling, CNN, QNN, and hybrid QqNN architectures is provided in Supplementary Material Sect. S1, together with important and necessary python code snippets and explanations to facilitate reproducibility.

Bit-error-rate–driven evaluation of compensation fidelity

To rigorously quantify the information-preserving capacity of the proposed compensation frameworks, we adopted a BER–based metric mapped onto a symbol-encoded OAM alphabet[62]. Each topological charge $l \in \{1,4,8,12\}$ was assigned a unique two-bit representation (00, 01, 10, 11), thereby allowing BER to serve as a

Model	Trainable parameters	Training time / Epoch	Inference time / Batch
CNN	$\sim 1.2 \times 10^5$	~0.8 s	~0.12 s
QNN	$\sim 7.3 \times 10^4$	~2.6 s	~0.38 s
QqNN	$\sim 9.1 \times 10^4$	~1.7 s	~0.20 s

Table 1. Comparative analysis of computational complexity metrics across neural network architectures.

direct measure of communication fidelity. A CNN classifier was first trained exclusively on ground-truth LG beams to ensure the network learned the ideal, uncorrupted mode characteristics[16,63,64]. Using GT beams for training is standard practice in OAM-based communication systems, as it provides a reliable reference for evaluating the efficacy of compensation schemes and ensures that any subsequent BER measurement reflects deviations caused solely by channel distortions rather than limitations of the classifier[16,63]. The CNN architecture comprised three convolutional stages (16–16–32 filters) with interleaved batch normalization, ReLU activations, max/average pooling, and dropout regularization, followed by a dense layer with four units and a softmax output[9]. Hyperparameters included an Adam optimizer (learning rate = 10^{-4}), mini-batch size of 50, and 20 epochs, consistent with architectures previously validated for OAM beam classification tasks[9,10]. The CNN BER-evaluation training curves for both simulation and experiment are nearly identical, confirming reproducibility as shown in Supplementary Fig. 2.

After training on GT, this network served as a decoding benchmark to infer symbol decisions for (i) distorted beams without compensation, and (ii) compensated beams reconstructed by CNN, QNN, and QqNN models. The predicted sequences were compared against the transmitted bit sequences to extract BER, total error counts, and classification accuracy. This testing methodology is widely recognized in optical communication research as it provides a standardized and efficient protocol to assess system-level performance, allowing direct comparison of compensation strategies under identical conditions. Both simulation datasets and experimental tabletop measurements were evaluated to provide a dual-layer validation of the compensation performance.

Experimental implementation of multi-physics structured-light propagation

To validate the numerical simulations and assess the fidelity of OAM beam reconstruction under realistic channel impairments, a tabletop optical experiment was devised to emulate sequential multiphysics degradations. The experimental framework replicates a free-space quantum communication channel, encompassing three principal distortion stages: atmospheric turbulence, volumetric scattering (fog), and quantum decoherence (dephasing and photon loss). A coherent He–Ne laser (Melles-Griot 05-LHP123–496, CW, 5 mW, 1 mm spot size) provided the linearly polarized input, ensuring optimal phase modulation on liquid-crystal-based Spatial Light Modulators (SLMs). The first SLM (SLM1) generated the target LG mode by encoding the desired azimuthal index with an additional phase-blaze grating to diffract the beam into a clean first-order mode, subsequently filtered by a pinhole to remove higher diffraction orders. The resulting beam represents the input modal state of interest for the multiphysics channel. SLM2 implements phase perturbations corresponding to Kolmogorov turbulence, physically reproducing atmospheric refractive-index fluctuations. High- and low-frequency components of the phase screen are synthesized via FFT-based methods and subharmonic generation, then resized to the SLM resolution to emulate the statistical characteristics of turbulent propagation as defined in Sect. II.

The third SLM (SLM3) simultaneously encodes fog-induced volumetric scattering and quantum-level decoherence. Fog scattering is represented by a phase-only approximation of the inverse Fourier transform of a Gaussian PSF derived from the Henyey–Greenstein model, reproducing the angular broadening observed in dense fog. Dephasing noise is implemented by applying stochastic phase shifts at randomly selected spatial coordinates according to a Bernoulli distribution with probability γ_d, while amplitude damping (photon loss) is emulated through strong local phase scrambling at sites determined probabilistically by γ_l. Complementary global photon attenuation is realized via a calibrated beam splitter after SLM3. The modulated beam is subsequently collected and imaged onto a CCD camera, capturing intensity and mode structure for direct comparison with simulations. Although turbulence, scattering, and quantum decoherence are applied sequentially via SLM2, SLM3, and a beam splitter, the cumulative field emerging at the detector naturally incorporates coupling effects between all distortion stages, capturing phase–amplitude interactions, modal crosstalk, and turbulence-modulated scattering, thereby faithfully reproducing realistic multiphysics channel conditions. For dataset construction, 1000 images per topological charge class were recorded for both fully perturbed beams and unperturbed ground-truth beams, yielding a total of 4000 experimental inputs and 4000 corresponding reference images. This dual dataset enables rigorous verification of simulation fidelity and benchmarking of classical, quantum, and hybrid reconstruction models. The laboratory implementation of the multiphysics channel and compensation pipeline is shown in Fig. 3.

Results of the proposed system

We present a comprehensive quantitative and qualitative assessment of the proposed OAM compensation strategies, summarized in Table 2 and illustrated in Figs. 4 and 5 for numerical simulations and experimental datasets, respectively. Across all topological charges, a clear hierarchy emerges: the variational QNN consistently achieves near-ideal reconstruction fidelity, closely followed by the QqNN, whereas classical CNN performance deteriorates markedly with increasing vortex order. For low-order modes (l=1), the CNN achieves moderate recovery (simulation SSIM = 0.899, experimental SSIM = 0.809), whereas QNN attains near-perfect fidelity (SSIM > 0.998), and QqNN provides intermediate restoration (simulation SSIM = 0.943, experimental SSIM = 0.951), demonstrating its efficacy as a computationally tractable surrogate. With increasing complexity (l=4), CNN performance declines (SSIM ≈ 0.818), while QNN remains virtually unaffected (SSIM = 0.998) and QqNN continues to deliver high-fidelity recovery (simulation SSIM = 0.957, experimental SSIM = 0.991). At intermediate (l=8) and high-order (l=12) modes, CNN reconstructions collapse (simulation SSIM = 0.366, 0.018; experimental SSIM = 0.618, 0.431), whereas QNN demonstrates remarkable resilience (simulation SSIM = 0.998–0.999, experimental SSIM = 0.988–0.994), and QqNN maintains near-quantum performance (simulation SSIM = 0.946–0.972, experimental SSIM = 0.990–0.996), reflecting its capability to emulate entanglement-enhanced tensor projections and mitigate nonlinear modal scrambling.

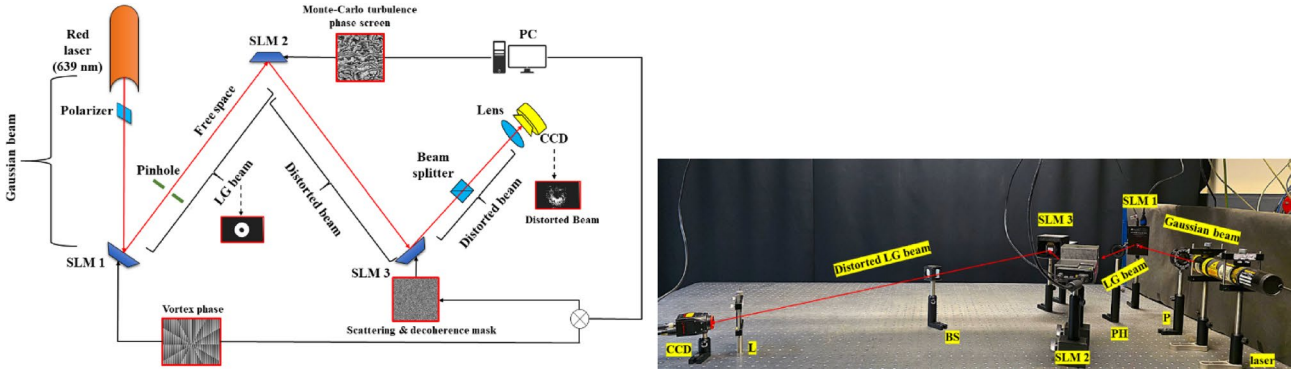

Fig. 3. Laboratory tabletop experiment: Experimental configuration for validating beam compensation. A laser source is passed through a polarizer (P) and SLM1 to generate LG modes. The beam is subsequently propagated through SLM2 (Monte Carlo turbulence phase screen), SLM3 (fog scattering and quantum decoherence emulation), followed by a beam splitter (BS) introducing global photon loss. A collection lens (L) directs the perturbed beam onto a camera for post-processing.

Topological charge	Model	Simulation			Experiment		
		MSE	RMSE	SSIM	MSE	RMSE	SSIM
1	CNN	0.001812	0.04257	0.899	0.005433	0.0737	0.809
	QNN	7.00×10^{-6}	0.00267	0.999	1.1×10^{-4}	0.0104	0.998
	QqNN	1.45×10^{-4}	0.01203	0.943	2.9×10^{-4}	0.0172	0.951
4	CNN	0.006204	0.07877	0.818	0.011178	0.105728	0.817
	QNN	4.00×10^{-6}	0.00197	0.998	1.6×10^{-4}	0.012812	0.998
	QqNN	3.80×10^{-5}	0.00616	0.957	1.4×10^{-4}	0.011999	0.991
8	CNN	0.012422	0.11146	0.366	0.028223	0.167997	0.618
	QNN	1.20×10^{-5}	0.00343	0.998	1.7×10^{-4}	0.013357	0.988
	QqNN	2.50×10^{-5}	0.00500	0.946	5.0×10^{-5}	0.007055	0.990
12	CNN	0.018689	0.13671	0.511	0.050604	0.224954	0.431
	QNN	2.20×10^{-5}	0.00470	0.999	1.7×10^{-4}	0.013358	0.994
	QqNN	1.90×10^{-5}	0.00433	0.972	4.6×10^{-5}	0.006805	0.996

Table 2. Quantitative decoding metrics: structural similarity index (SSIM), mean-squared error (MSE), and root-mean-squared error (RMSE) across simulation and experiment for $l = 1, 4, 8, 12$.

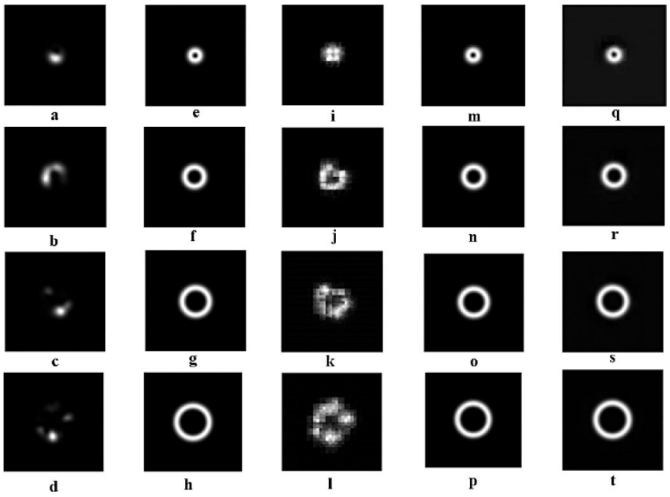

Fig. 4. Simulation results of LG beam compensation: Columns show: input beams (**a**–**d**), ground truth beams (**e**–**h**), CNN-reconstructed beams (**i**–**l**), QNN reconstructions (**m**–**p**), and QqNN reconstructions (**q**–**t**). Rows correspond to topological charges $l = 1, 4, 8$, and 12.

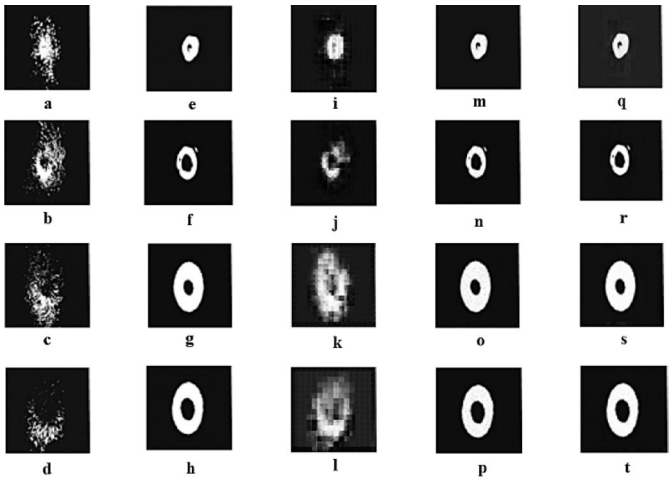

Fig. 5. Experimental results of LG beam compensation: Columns follow the same format as Fig. 4 (input, ground truth, CNN, QNN, QqNN), for topological charges $l = 1$, 4, 8, and 12.

Qualitative inspection of Figs. 4 and 5 corroborates these trends: CNN reconstructions exhibit blurred vortex cores and distorted intensity patterns at higher charges, whereas QNN and QqNN maintain structural fidelity, with only minor deviations in intensity uniformity for the hybrid model. These results underscore the quantum-inspired networks' superior robustness against multi-physics perturbations including turbulence, scattering, and quantum-limited noise.

Training behavior analysis

Analysis of training dynamics further emphasizes the scalability and efficiency of quantum-informed architectures. Across all topological charges, QNN and QqNN converge to final training losses over 99% lower than the CNN, demonstrating orders-of-magnitude improvements in reconstruction efficiency. While all models showed effective convergence with decreasing loss over 20 epochs, the quantum-inspired models consistently achieved final loss values several orders of magnitude lower than the CNN. In simulation, the QNN and QqNN models achieved average final losses of 0.000025 and 0.000063, respectively, compared to the CNN's average of 0.009812, representing a mean performance improvement exceeding 99%. This trend was strongly maintained in the experimental data, despite higher overall loss values for all models due to real-world noise and environmental factors. Here, the QNN and QqNN's average final losses of 0.000191 and 0.000148 were more than 99% better than the CNN's average of 0.024296. Representative convergence trends for $l = 4$ are shown in Fig. 6. Additional cases are provided in Supplementary Fig. 3.

For instance, in the simulation, the CNN's loss increased from 0.001802 (charge 1) to 0.018401 (charge 12), but the QNN and QqNN models maintained a minimal loss throughout, consistently achieving values below 0.0002. This indicates that while the CNN's performance degrades as the complexity of the OAM topological charge increases, the QNN and QqNN architectures remain robust and highly effective. Second, a clear trend is observed across the models' performance as the topological charge increases: as the complexity of the OAM beam grows, the CNN's final loss shows a marked increase in both simulation (from 0.001802 to 0.018401) and experiment (from 0.005242 to 0.050515). In contrast, the QNN and QqNN models demonstrate a remarkable stability, with their final loss values remaining consistently low, regardless of the topological charge. For example, the QNN's final loss in the simulation only increased from 0.000010 for charge 1 to 0.000030 for charge 12. This suggests that the quantum-inspired models are fundamentally more adept at handling the escalating complexity of higher-order OAM beams, making them a more scalable and superior solution for real-world applications.

Comparative BER and accuracy analysis in simulation and experiment

The BER and accuracy statistics, obtained across 8,000 transmitted bits per scenario, reveal a consistent hierarchy in compensation performance. Communication-level performance metrics are reported in Table 3.

In simulation, uncompensated beams yielded an accuracy of 39.3% with a BER of 0.398 (≈ 3,184-bit errors). CNN-based compensation improved mode integrity to 86.15% accuracy with BER reduced to 0.116 (≈ 928 errors). The QNN demonstrated near-perfect recovery with 99.98% accuracy and a BER of 0.000125 (≈ 1 error), while the QqNN achieved 99.95% accuracy and BER of 0.00037 (≈ 3 errors). In the experimental tabletop setup, which incorporated physical turbulence and scattering, the trends were reproduced: uncompensated beams reached 45.7% accuracy with BER = 0.412 (≈ 3,296 errors), CNN compensation achieved 88.10% accuracy with BER = 0.059 (≈ 472 errors), QNN again delivered 99.98% accuracy with BER = 0.00012 (≈ 1 error), and QqNN achieved 99.95% accuracy with BER = 0.00025 (≈ 2 errors). Notably, both QNN and QqNN reduced BER by more than three orders of magnitude compared to distorted inputs, with confusion matrices showing nearly ideal diagonality, confirming the preservation of OAM mode integrity after quantum-informed reconstruction. This dual assessment across simulation and experimental platforms validates the reliability and efficiency of

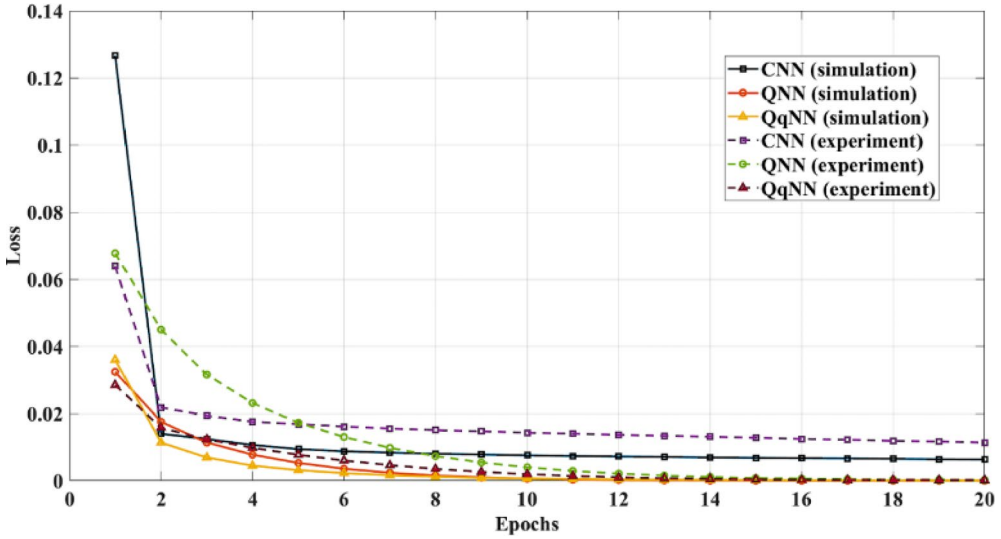

Fig. 6. Training convergence for $l = 4$: Training loss curves for CNN, QNN, and QqNN under both simulation and experiment. The QNN and QqNN converge to > 99% lower final loss relative to CNN, highlighting the advantage of quantum-enhanced feature learning.

Models	Simulation		Experiment	
	BER	Accuracy	BER	Accuracy
Uncompensated beams	0.398	39.3%	0.412	45.7%
Compensated beams using CNN	0.116	86.15%	0.0595	88.1%
Compensated beams using QNN	1.2×10^{-4}	99.98%	1.2×10^{-4}	99.98%
Compensated beams using QqNN	3.7×10^{-4}	99.95%	2.5×10^{-4}	99.95%

Table 3. BER and classification accuracy: Bit-error-rate (BER) and symbol decoding accuracy for uncompensated beams and for compensation using CNN, QNN, and QqNN.

using GT-trained CNNs as a standardized decoding benchmark. The effect of beam compensation on simulated communication capacity is presented in Fig. 7 and experimental communication performance is shown in Fig. 8.

Discussion and conclusion

The present study establishes a new benchmark in distortion-resilient optical beam decoding by demonstrating, for the first time, the efficacy of fully parameterized QNNs and QqNNs for reconstructing OAM beams under compound propagation impairments—conditions directly relevant to free-space optical links, multimode fibers, and integrated photonic waveguides. While CNNs have previously been employed for turbulence compensation in classical optical systems, their performance degrades significantly in high-noise, strongly nonlinear regimes, particularly for beams with high topological charges (l). In contrast, our QNN achieved sub-10^{-5} MSE and SSIM ≈ 0.999 for l up to 12 in simulation and SSIM ≈ 0.994 experimentally, thereby demonstrating an order-of-magnitude improvement over CNN-based counterparts (Table 2). A clear topological charge–dependent performance trend emerged. For $l = 1$, all models performed reasonably well (SSIM > 0.80 experimentally). However, as l increased, CNNs rapidly lost reconstruction fidelity (dropping to SSIM = 0.431 for $l = 12$), whereas QNNs retained near-ideal decoding (SSIM = 0.999 in simulation, 0.994 experimentally). This resilience is attributed to the ability of QNNs to exploit the high-dimensional Hilbert space and quantum entanglement to capture nonclassical spatial correlations—features that classical CNNs fail to disentangle under modal decoherence, turbulence-induced beam wander, or modal crosstalk in multimode fibers and waveguides. The results are consistent with the physics of high-order OAM beams, where larger ring radii and sharper phase gradients increase sensitivity to scattering and turbulence.

The QqNN model, introduced in this work, offers a compelling hybrid alternative. By combining classical convolutional preconditioners with shallow quantum variational circuits, it reduced quantum resource demands while achieving SSIM = 0.972 (simulation) and 0.996 (experiment) at $l = 12$, only marginally below the QNN. Its lower gate depth and reduced qubit requirements make it significantly more hardware-friendly for deployment on noisy intermediate-scale quantum (NISQ) processors and integration into fiber- and waveguide-based optical communication testbeds. This highlights the QqNN not merely as a reduced-complexity surrogate, but as a viable framework for real-time quantum-enhanced optical inference. While the primary analysis focused on four representative OAM charges (l = 1, 4, 8, 12), supplementary simulations were conducted for intermediate

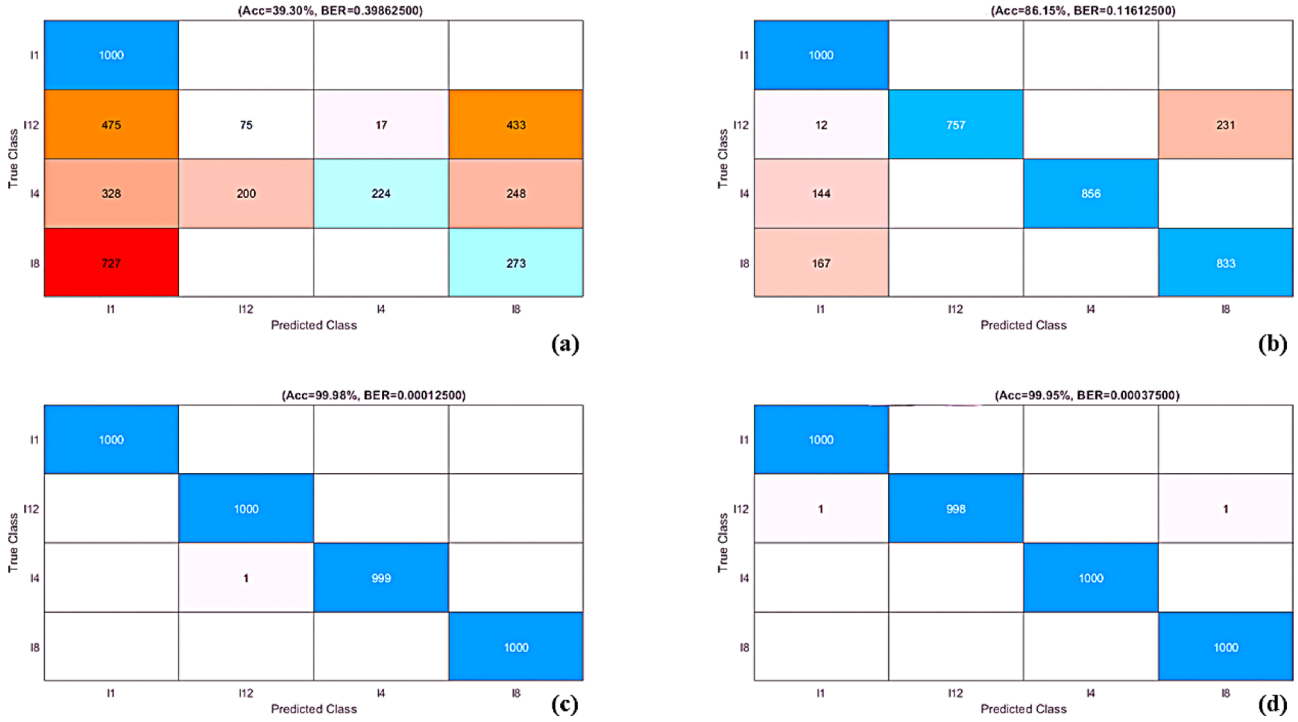

Fig. 7. Bit-error rate (BER) analysis in simulation: (**a**) uncompensated LG beam, (**b**) compensated beam via CNN, (**c**) via QNN, and (**d**) via QqNN.

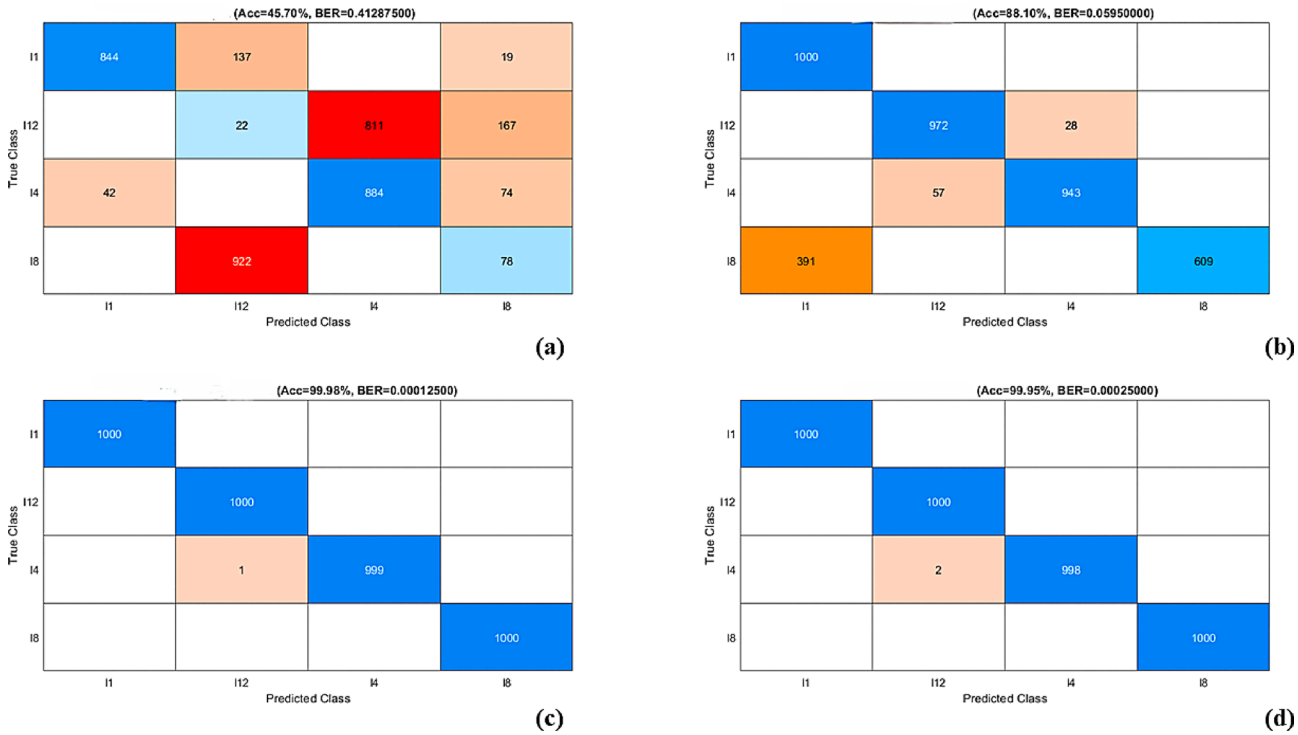

Fig. 8. Bit-error rate (BER) analysis in experiment: (**a**) uncompensated LG beam, (**b**) compensated beam via CNN, (**c**) via QNN, and (**d**) via QqNN.

charges (l = 2, 3, 5, 6, 7, 10, 11) to confirm monotonic performance trends (illustrated in Supplementary Table 1). Reconstruction fidelity remains high for both QNN and QqNN (SSIM > 0.97–0.99), whereas CNN performance gradually declines with increasing l. The symmetric behavior observed for ± l is consistent with the invariance of intensity distributions under the transformation $l \rightarrow -l$[65]. For higher orders (l > 12), QNN and QqNN maintain robust performance (SSIM > 0.97 up to l = 16), whereas CNN performance deteriorates sharply (SSIM < 0.4), consistent with observations on modal crosstalk and turbulence sensitivity reported in recent studies[66,67].

From a communication standpoint, BER metrics further corroborate the superiority of quantum learning models. Uncompensated beams exhibited BER ≈ 0.398–0.412 with accuracy < 46%, rendering them unsuitable for reliable transmission (Table 3). CNN compensation improved accuracy to 86–88%, but QNN and QqNN dramatically reduced BER to the 10^{-4} level (0.00012–0.00037), corresponding to decoding accuracies above 99.95% in both simulation and experiment. This places our system an order of magnitude ahead of conventional optical-turbulence compensation approaches (typically reported near 10^{-3})[18] and provides a pathway toward telecom-grade reliability in both FSO and guided-wave optical links. Although the BER values remain marginally above the stringent 10^{-5} benchmark for telecom-grade systems due to the limited two-bit OAM encoding scheme, expansion to larger mode alphabets would exponentially suppress normalized BER and push the system into the ultra-reliable communication regime. The demonstrated reproducibility between simulation and tabletop validation confirms that quantum neural architectures offer a practically deployable pathway to robust, high-capacity, and noise-resilient OAM-based optical communication.

Comparison with prior works

To quantitatively situate our approach within the broader literature, we benchmarked the mean Structural Similarity Index Measure (SSIM) values of our CNN-, QNN-, and QqNN-based reconstruction models against recent state-of-the-art turbulence compensation studies (Supplementary Fig. 4). SSIM is a standard perceptual metric for assessing image reconstruction quality, comparing luminance, contrast, and structural information between reference and reconstructed images. Although SSIM offers a useful measure of fidelity, direct comparison across studies can be misleading, as differences in datasets, turbulence strength, and evaluation protocols strongly affect the metric. Our quantum-inspired frameworks consistently outperform conventional CNNs and recent deep-learning approaches by Tan Qu et al. (2023)[14] and Zhi Zhang et al. (2024, 2025)[18,68]. The QNN achieved mean SSIM values of 0.998 (simulation) and 0.994 (experiment), significantly higher than typical CNN-only results under turbulence (≈ 0.65). The QqNN exhibited comparably strong performance, with mean SSIMs of 0.954 (simulation) and 0.983 (experiment), surpassing most turbulence-only benchmarks and approaching the best reported results. While our SSIM values demonstrate high-fidelity reconstruction, numerical comparisons with prior works should be interpreted cautiously. The key advantage of our quantum-inspired models lies in their ability to jointly compensate for multiple channel impairments, preserve OAM-mode fidelity across diverse conditions, and provide scalable hybrid architectures suitable for near-term quantum hardware.

Interestingly, when compared against compensation studies in underwater turbulence (Peng Hu et al. 2024, SSIM ≈ 0.9531[69]; Silei Wu et al. 2024, SSIM ≈ 0.978[70]; Jiao Wang et al. 2025, SSIM ≈ 0.7329[71], our QNN and QqNN results demonstrate comparable or superior fidelity, despite addressing a more challenging multi-distortion propagation scenario. These cross-domain comparisons emphasize the robustness and universality of our proposed architectures. Beyond performance metrics, it is instructive to contrast our framework with recent methodologies addressing OAM distortion compensation. Most contemporary approaches have been rooted in classical or hybrid deep-learning architectures, adaptive optics (AO), or generative adversarial networks (GANs), whereas our framework introduces a fundamentally different paradigm by exploiting the quantum feature space.

GAN-based approaches: Tan Qu et al. (2023)[14] applied an improved CycleGAN to turbulence-distorted vortex beams, framing compensation as an image-to-image translation problem. Their method improved recognition accuracy by 4.4% compared to uncompensated beams, with SSIM values approaching unity. Similarly, Zhi Zhang et al. (2024, 2025)[18,68] extended Pix2PixGAN to turbulence compensation in OAM-based FSOC systems. In the 2024 work, the GAN directly recovered turbulence phase screens, improving Strehl ratios by up to 35.7% and mode recognition to > 99%. The 2025 study proposed a sensor-less AO scheme using GANs, eliminating the need for wavefront sensors while achieving BER ≈ 10^{-3} in an 80 Gbit/s OAM link. These studies confirm GANs' capacity to learn complex turbulence-induced mappings. However, GANs often suffer from training instability, mode collapse, and heavy data requirements. In contrast, our quantum-inspired QNN/QqNN models leverage high-dimensional quantum feature spaces, enabling compact parameterization and stable convergence with smaller datasets. Under comparable turbulence conditions, our QqNN achieved BER < 10^{-4} in simulation, illustrating the potential of hybrid quantum–classical learning to outperform data-intensive GAN frameworks in both efficiency and reconstruction fidelity.

Deep-learning AO hybrids: Huan Chang et al. (2024)[17] proposed a Y-net aided AO method, achieving high-accuracy distortion compensation without probe paths, emphasizing reduced complexity compared to CNN-based AO. Similarly, Yue Xu et al. (2023)[72] implemented an AO pre-compensation scheme using beacon-based wavefront sensing, achieving ~ 12.6 dB power penalty improvement and 6 dB reduction in modal crosstalk. These works underscore the practical importance of AO-based pre-compensation, but both rely on hardware wavefront corrections, introducing complexity not present in our purely computational framework. CNN–residual architectures: Yuhang Wu et al. (2023)[32] integrated convolutional and residual blocks for turbulence phase prediction in multiplexed OAM links. Their approach achieved > 10 dB power improvement under turbulence, with significant crosstalk reduction. However, as with most CNN-based models, performance degrades under high-l modes or severe compound distortions, precisely where our QNN retains near-perfect decoding (SSIM > 0.99 at l = 12). A detailed comparative analysis of turbulence-compensated SSIM performance across simulation, experiment, and prior studies is provided in Table 4, underscoring the robustness and generalizability of our quantum neural models.

Study	Method	Distortion type	Reported metric	Advantages	Limitations
Tan Qu et al. (2023)[14]	CycleGAN with SSIM loss	Atmospheric turbulence	SSIM ≈ 0.94; +4.4% accuracy gain	End-to-end compensation without hardware	GAN instability; limited to turbulence
Zhi Zhang et al. (2024)[68]	Pix2PixGAN	Atmospheric turbulence	Strehl ↑ 35.7%; Mode accuracy > 99%	Direct recovery of phase screens; high mode fidelity	Requires large training data; turbulence-only
Zhi Zhang et al. (2025)[18]	Sensor-less AO via Pix2PixGAN	Severe turbulence ($D/r_0 = 8$)	BER ≈ 10^{-3}; Power ↑ 3.7 dBm	Removes wavefront sensor; works under strong turbulence	BER plateau at 10^{-3}; limited scalability
Huan Chang et al. (2024)[17]	Y-net AO (non-probe)	Turbulence	High-accuracy compensation; robust demodulation	Low structural complexity; no probe path	Still AO-dependent; CCD path required
Yue Xu et al. (2023)[72]	AO pre-compensation	Turbulence	Power penalty ↓ 12.6 dB; Crosstalk ↓ 6 dB	Real-time pre-compensation feasible	Requires beacon hardware; turbulence-only
Yuhang Wu et al. (2023)[32]	CNN; residual blocks	Turbulence in multiplexed OAM links	Power ↑ 10 dB; Crosstalk ↓ 10 dB	Fast prediction; good for multiplexing	Accuracy drops at high l; classical limits remain
This work (2025)	QNN; QqNN	Strong turbulence; Fog; Quantum noise	SSIM = 0.994–0.999; BER = $1.2–3.7 \times 10^{-4}$	Quantum-native decoding; robust at high l; no AO hardware needed	Requires quantum simulation; hardware integration pending

Table 4. Comparative benchmark of turbulence-compensated image reconstruction fidelity: reported mean SSIM values of our CNN-, QNN-, and QqNN-based models (simulation and experiment) are juxtaposed against leading turbulence compensation frameworks from prior works. The table highlights the consistent superiority of quantum-enabled models across both simulated and experimental settings.

Taken together, these studies highlight the incremental advances achievable through classical or GAN-based learning. By contrast, our QNN/QqNN approach departs methodologically, leveraging the quantum Hilbert space to encode and disentangle high-order spatial correlations without relying on phase retrieval, AO hardware, or adversarial training. This enables record-low BER (10^{-4} range), near-ideal SSIM values (0.994–0.999), and scalability to high topological charges under compound turbulence, fog, and quantum noise, which no prior study has simultaneously addressed.

Novelty, impact, and future directions

To our knowledge, this study is the first to implement a fully parameterized QNN for OAM beam compensation under multi-channel distortions, including turbulence, fog scattering, and quantum noise. We also introduce a quantum-classical hybrid neural network (QqNN) that achieves near-QNN-level performance while remaining NISQ-compatible. Our research provides a physically rigorous simulation testbed incorporating Rytov-parameter-based turbulence ($C_n^2 = 10^{-13}$ $m^{-2/3}$, $L_0 = 100$ m), fog-induced extinction ($\beta = 3.912/50$ m^{-1}), and quantum noise channels (phase damping and photon loss). By achieving a BER in the 10^{-4} range, this work sets a new quantitative standard for turbulence-compensated OAM links. This research opens several pathways for future work: extending the framework to OAM superpositions and entangled photon pairs to enable quantum-secure multiplexing; integrating quantum kernel methods and quantum convolutional layers for more compact architectures; and envisioning hardware-in-the-loop training on real quantum devices to accelerate the realization of quantum-enhanced free-space optical communication, mode-division multiplexing in multimode fibers, integrated waveguide interconnects, and satellite-to-ground quantum links. In summary, our findings demonstrate that quantum machine learning architectures—particularly QNNs and QqNNs—substantially outperform classical deep learning models in reconstructing complex Laguerre–Gaussian OAM modes under realistic environmental distortions. By achieving near-ideal SSIM values and record-low BERs, this study sets a new benchmark in optical compensation and establishes a foundation for future quantum-enhanced photonic communication systems.

Data availability

The dataset and codes for this study will be presented upon reasonable request to the corresponding author, Gokul Manavalan (gokulm@post.bgu.ac.il).

Received: 7 September 2025; Accepted: 28 November 2025
Published online: 02 December 2025

References

1. MG Zhou ZP Liu HL Yin CL Li TK Xu ZB Chen 2023 Quantum neural network for quantum neural computing Research https://doi.org/10.34133/research.0134
2. Y Qian X Wang Y Du X Wu D Tao 2024 The dilemma of quantum neural networks IEEE Trans. Neural Netw. Learn. Syst. 35 4 5603 5615 https://doi.org/10.1109/TNNLS.2022.3208313
3. S Monaco O Kiss A Mandarino S Vallecorsa M Grossi 2023 Quantum phase detection generalization from marginal quantum neural network models Phys. Rev. B 107 8 L081105 https://doi.org/10.1103/PhysRevB.107.L081105
4. Y Kwak WJ Yun S Jung J Kim 2021 Quantum neural networks: concepts, applications, and challenges 2021 Twelfth International Conference on Ubiquitous and Future Networks (ICUFN) IEEE 413 416 https://doi.org/10.1109/ICUFN49451.2021.9528698
5. Y Lian X Qi Y Wang Z Bai Y Wang Z Lu 2022 OAM Beam Generation in Space and its Applications: A Review Elsevier https://doi.org/10.1016/j.optlaseng.2021.106923
6. Y Lian X Qi Y Wang Z Bai Y Wang Z Lu 2022 OAM beam generation in space and its applications: A review Opt. Lasers Eng. 151 106923 https://doi.org/10.1016/j.optlaseng.2021.106923

7. X Chen 2025 Two novel mechanisms for suppressing higher-order radial modes in dual-ring core hollow-core fibers for OAM transmission J. Lightwave Technol. https://doi.org/10.1109/JLT.2025.3597082
8. W Geng 2025 Generation of dispersive waves in double-ring core fiber for high-order OAM modes IEEE J. Quantum Electron https://doi.org/10.1109/JQE.2025.3598606
9. G Manavalan GM Balasubramaniam S Arnon 2025 Improving OAM-based optical wireless communication in turbulence using conjugate light field and hybrid neural networks J. Lightwave Technol. 43 7 3211 3221 https://doi.org/10.1109/JLT.2024.3517712
10. GM Balasubramaniam R Kumar S Arnon 2024 Vortex beams and deep learning for optical wireless communication through turbulent and diffuse media J. Lightwave Technol. 42 10 3631 3641 https://doi.org/10.1109/JLT.2024.3362255
11. Q Ding 2022 Design and performance analysis of hybrid multidimensional OAM-DM-WDM-OFDM-PON system with high-capacity and long-distance transmission Photonics https://doi.org/10.3390/photonics9070448
12. L Zhu M Deng B Lu X Guo A Wang 2023 Turbulence-resistant high-capacity free-space optical communications using OAM mode group multiplexing Opt. Express 31 9 14454 https://doi.org/10.1364/OE.488053
13. Q Jia 2022 Compensating the distorted OAM beams with near zero time delay Appl. Phys. Lett. https://doi.org/10.1063/5.0096303
14. T Qu Y Zhang J Wu Z Wu 2023 Vortex beam transmission compensation in atmospheric turbulence using CycleGAN Photonics 10 11 1182 https://doi.org/10.3390/photonics10111182
15. S Li S Chen C Gao AE Willner J Wang 2018 Atmospheric turbulence compensation in orbital angular momentum communications: Advances and perspectives Opt. Commun. 408 68 81 https://doi.org/10.1016/j.optcom.2017.09.034
16. Y Guo L Li J Wang C Gao S Fu 2023 Distortion compensation for orbital angular momentum beams: from probing to deep learning J. Lightwave Technol. 41 7 2041 2050 https://doi.org/10.1109/JLT.2022.3218828
17. H Chang P Xu H Yao J Li X Xin M Guizani 2024 Nonprobe adaptive compensation for optical wireless communications based on orbital angular momentum IEEE Trans. Wirel. Commun. 23 8 9033 9043 https://doi.org/10.1109/TWC.2024.3357737
18. Z Zhang 2025 Turbulence compensation based on pix2pixGAN for the free-space optical communication of orbital angular momentum multiplexing Appl. Opt. 64 5 A1 https://doi.org/10.1364/AO.535452
19. T Haug K Bharti MS Kim 2021 Capacity and quantum geometry of parametrized quantum circuits PRX Quantum 2 4 040309 https://doi.org/10.1103/PRXQuantum.2.040309
20. M Larocca N Ju D García-Martín PJ Coles M Cerezo 2023 Theory of overparametrization in quantum neural networks Nat. Comput. Sci. 3 6 542 551 https://doi.org/10.1038/s43588-023-00467-6
21. Z Qu Y Li P Tiwari 2023 QNMF: A quantum neural network based multimodal fusion system for intelligent diagnosis Inf. Fus. 100 101913 https://doi.org/10.1016/j.inffus.2023.101913
22. E Paquet F Soleymani 2022 QuantumLeap: Hybrid quantum neural network for financial predictions Expert Syst. Appl. 195 116583 https://doi.org/10.1016/j.eswa.2022.116583
23. B Merabet L Li SAA Shah Z Guo 2025 Quantum neural network boosting identifying orbital angular momentum modes Adv. Quantum Technol. https://doi.org/10.1002/qute.202400680
24. S Pachava 2019 Generation and decomposition of scalar and vector modes carrying orbital angular momentum: a review Opt. Eng. 59 04 1 https://doi.org/10.1117/1.oe.59.4.041205
25. A Papathanasopoulos Y Rahmat-Samii 2021 Fundamentals of orbital angular momentum beams A Papathanasopoulos Y Rahmat-Samii Eds Electromagnetic Vortices Wiley 1 32 https://doi.org/10.1002/9781119662945.ch1
26. Y-D Liu X Yang J Wang R Wang Y Yang 2024 Orthogonality of non-coaxial Laguerre-Gaussian beams Opt. Express 32 4 4876 https://doi.org/10.1364/OE.510662
27. Z Guo Z Wang MI Dedo K Guo 2018 The orbital angular momentum encoding system with radial indices of Laguerre-Gaussian beam IEEE Photonics J. https://doi.org/10.1109/JPHOT.2018.2859807
28. Y Li Y Han Z Cui J Wang W Zhao 2020 Simultaneous identification of the azimuthal and radial mode indices of Laguerre-Gaussian beams using a spiral phase grating J. Phys. D Appl. Phys. 53 8 085106 https://doi.org/10.1088/1361-6463/ab5d51
29. A Trichili MA Cox B Perez-Garcia BS Ooi M Alouini 2021 Theory and practice of orbital angular momentum and beyond A Trichili MA Cox B Perez-Garcia BS Ooi M Alouini Eds Digital Encyclopedia of Applied Physics Wiley 1 32 https://doi.org/10.1002/3527600434.eap949
30. Z Li J Su X Zhao 2020 Atmospheric turbulence compensation with sensorless AO in OAM-FSO combining the deep learning-based demodulator Opt. Commun. 460 125111 https://doi.org/10.1016/j.optcom.2019.125111
31. J Li M Zhang D Wang S Wu Y Zhan 2018 Joint atmospheric turbulence detection and adaptive demodulation technique using the CNN for the OAM-FSO communication Opt. Express 26 8 10494 https://doi.org/10.1364/OE.26.010494
32. Y Wu A Wang L Zhu 2023 Direct prediction and compensation of atmospheric turbulence for free-space integer and fractional order OAM multiplexed transmission links Opt. Express 31 22 36078 https://doi.org/10.1364/OE.501510
33. J Delpiano GL Funes JE Cisternas S Galaz JA Anguita 2019 Deep learning for image-based classification of OAM modes in laser beams propagating through convective turbulence SPIE Intl. Soc. Opt. Eng https://doi.org/10.1117/12.2529303
34. JD Schmidt 2010 Numerical simulation of optical wave propagation with examples in MATLAB SPIE https://doi.org/10.1117/3.866274
35. G Manavalan S Arnon 2024 Propagation of structured gaussian beams through strong turbulence G Manavalan S Arnon Eds 2024 IEEE International Conference on Microwaves, Communications, Antennas, Biomedical Engineering and Electronic Systems (COMCAS) IEEE 1 5 https://doi.org/10.1109/COMCAS58210.2024.10666253
36. M Kolářová L Lachiver A Wilkie 2024 An empirically derived adjustable model for particle size distributions in advection fog Comput. Graph. Forum https://doi.org/10.1111/cgf.15008
37. J Jendersie E d'Eon 2023 An approximate mie scattering function for fog and cloud rendering J Jendersie E d'Eon Eds ACM SIGGRAPH 2023 Talks ACM 1 2 https://doi.org/10.1145/3587421.3595409
38. H Koklu 2025 Calculation of radiative thickness using spherical harmonic methods for the radiative transfer equation Front. Phys. https://doi.org/10.3389/fphy.2025.1570080
39. X Bai 2023 Analysis of the effect of optical thickness on polarization in a sea fog stratified environment Appl. Opt. 62 33 8749 https://doi.org/10.1364/AO.499987
40. H Pan S Ganeshan T Iadecola JH Wilson JH Pixley 2024 Local and nonlocal stochastic control of quantum chaos: Measurement- and control-induced criticality Phys. Rev. B 110 5 054308 https://doi.org/10.1103/PhysRevB.110.054308
41. J Dexter IJ Ford 2025 Stochastic entropy production for classical and quantum dynamical systems with restricted diffusion Entropy 27 4 383 https://doi.org/10.3390/e27040383
42. M Taleb 2025 Ultrafast phonon-mediated dephasing of color centers in hexagonal boron nitride probed by electron beams Nat. Commun. 16 1 2326 https://doi.org/10.1038/s41467-025-57584-1
43. K Berrada S Bougouffa 2025 Robustness of quantum correlations in photonic systems under non-Markovian dephasing: theoretical analysis in the experimental range Sci. Rep. 15 1 22260 https://doi.org/10.1038/s41598-025-06304-2
44. D Li 2025 Theoretical basis D Li Eds Quantum Teleportation under Noise Springer Nature 23 44 https://doi.org/10.1007/978-3-031-91250-4_2
45. B Khanal P Rivas 2024 A modified depolarization approach for efficient quantum machine learning Mathematics 12 9 1385 https://doi.org/10.3390/math12091385
46. Y-Y Hong 2024 Solar irradiance forecasting using a hybrid quantum neural network: a comparison on GPU-based workflow development platforms IEEE Access 12 145079 145094 https://doi.org/10.1109/ACCESS.2024.3472053

47. M Bourahla 2024 Quantum Convolution for Convolutional Neural Networks Springer 179 193 https://doi.org/10.1007/978-3-031-59318-5_14
48. UHM Zaman MA Arefin MA Akbar MH Uddin 2023 Utilizing the extended tanh-function technique to scrutinize fractional order nonlinear partial differential equations Part. Diff. Eq. Appl. Math. 8 100563 https://doi.org/10.1016/j.padiff.2023.100563
49. H. Cowlessur, T. Alpcan, C. Thapa, S. Camtepe, and N. K. Kundu, A qubit-efficient hybrid quantum encoding mechanism for quantum machine learning. (2025).
50. G Aubrun L Lami C Palazuelos M Plávala 2022 Entanglement and superposition are equivalent concepts in any physical theory Phys. Rev. Lett. 128 16 160402 https://doi.org/10.1103/PhysRevLett.128.160402
51. S. M. Y. I. Tomal, A. Al Shafin, A. Afaf, and D. Bhattacharjee, Quantum convolutional neural network: a hybrid quantum-classical approach for iris dataset classification. https://doi.org/10.62411/faith.3048-3719-48 (2024).
52. A Kadi A Selamnia ZA Houda El H Moudoud B Brik L Khoukhi 2025 an in-depth comparative study of quantum-classical encoding methods for network intrusion detection IEEE Open J. Commun. Soc. 6 1129 1148 https://doi.org/10.1109/OJCOMS.2025.3537957
53. FJ Duarte TS Taylor JC Slaten 2020 On the probability amplitude of quantum entanglement and the Pauli matrices Opt. Quantum Electron 52 2 106 https://doi.org/10.1007/s11082-020-2205-1
54. A Sakhnenko C O'Meara KJB Ghosh CB Mendl G Cortiana J Bernabé-Moreno 2022 Hybrid classical-quantum autoencoder for anomaly detection Quantum Mach. Intell. 4 2 27 https://doi.org/10.1007/s42484-022-00075-z
55. M Dutta 2024 Rice leaf disease classification—a comparative approach using convolutional neural network (CNN), cascading autoencoder with attention residual U-Net (CAAR-U-Net), and MobileNet-V2 architectures Technologies (Basel) 12 11 214 https://doi.org/10.3390/technologies12110214
56. C-W Liang C-C Chang C-Y Hsiao C-J Liang 2023 Prediction and analysis of atmospheric visibility in five terrain types with artificial intelligence Heliyon 9 8 e19281 https://doi.org/10.1016/j.heliyon.2023.e19281
57. S Cai Z Li Z Zhong B Zhang 2024 Deep-learning-based recognition of composite vortex beams through long-distance and moderate-to-strong atmospheric turbulence Phys. Rev. A (Coll Park) 110 1 013508 https://doi.org/10.1103/PhysRevA.110.013508
58. Y Jin C Zhou W Dai 2024 Long-range imaging through scattering media using deep learning Photonics 11 9 887 https://doi.org/10.3390/photonics11090887
59. J Liu 2019 Deep learning based atmospheric turbulence compensation for orbital angular momentum beam distortion and communication Opt. Express 27 12 16671 https://doi.org/10.1364/OE.27.016671
60. SK Gaire A Daneshkhah E Flowerday R Gong J Frederick V Backman 2024 Deep learning-based spectroscopic single-molecule localization microscopy J. Biomed. Opt. https://doi.org/10.1117/1.JBO.29.6.066501
61. J Chen P Li Y Wang P-C Ku Q Qu 2024 Sim2Real in reconstructive spectroscopy: Deep learning with augmented device-informed data simulation APL Mach. Learn. https://doi.org/10.1063/5.0209339
62. EE Elsayed MA Yakout AS Samra 2025 Atmospheric turbulence-resilient hybrid MIMO RF/FSO communication systems: adaptive *N* -SM and OAM-OMI assisted *M* -ary SPPM modulation with advanced diversity multiplexing for next-generation wireless networks J. Opt. Commun. https://doi.org/10.1515/joc-2025-0210
63. Y Guo L Li J Wang C Gao S Fu 2023 Distortion compensation for orbital angular momentum beams: from probing to deep learning J. Lightwave Technol. 41 7 2041 2050 https://doi.org/10.1109/JLT.2022.3218828
64. Z Li 2023 High-efficiency anti-interference OAM-FSO communication system based on Phase compression and improved CNN Opt. Commun. 537 129120 https://doi.org/10.1016/j.optcom.2022.129120
65. MA Cox T Celik Y Genga AV Drozdov 2022 Interferometric orbital angular momentum mode detection in turbulence with deep learning Appl. Opt. 61 7 D1 https://doi.org/10.1364/AO.444954
66. Z Zhao 2021 Modal coupling and crosstalk due to turbulence and divergence on free space THz links using multiple orbital angular momentum beams Sci. Rep. 11 1 2110 https://doi.org/10.1038/s41598-020-80179-3
67. NA Ferlic M Iersel van CC Davis 2021 Weak turbulence effects on different beams carrying orbital angular momentum J. Opt. Soc. Am. A 38 10 1423 https://doi.org/10.1364/JOSAA.432607
68. Z Zhang X Xie J Si W Wang S Jia D Gao 2024 Turbulence compensation with pix-to-pix generative adversarial networks in vector vortex beams Phys. Scr. 99 10 105532 https://doi.org/10.1088/1402-4896/ad74b8
69. P Hu 2024 Physics-driven untrained neural network for vortex beam compensation in adaptive optics aided underwater wireless optical communications Opt Express 32 27 47936 https://doi.org/10.1364/OE.541188
70. S Wu J Hu J Han 2024 Extraction and restoration method of underwater turbulence phase distortion information based on holographic interference P Zhou Eds AOPC 2024: Laser Technology and Applications SPIE 25 https://doi.org/10.1117/12.3046927
71. J Wang Y Wang Z Tan X Wang S Lei P Wu 2025 CNN-POT: predicting oceanic turbulence phase variations with convolutional neural networks J. Opt. 27 5 055401 https://doi.org/10.1088/2040-8986/adccd5
72. Y Xu B Lan C Liu M Chen A Tang H Xian 2023 Adaptive optics pre-compensation for orbital angular momentum beams transmitting through simulated atmospheric turbulence Opt. Express 31 9 13665 https://doi.org/10.1364/OE.473030

Author contributions

Conceptualization: GM, SAMethodology: GM, SA. Investigation: GM. Visualization: GM. Supervision: SA. Writing—original draft: GM. Writing—review & editing: GM, SA.

Funding

This research is funded by the Israel Science Foundation (ISF) under grant No. 897/21 - "Deep learning for multidimensional classification of complex structured light beams in optical wireless communication applications".

Declarations

Competing interests

The authors declare no competing interests.

Additional information

Supplementary Information The online version contains supplementary material available at https://doi.org/10.1038/s41598-025-31021-1.

Correspondence and requests for materials should be addressed to G.M.